

Article

An Approach for High-Resolution Mapping of Hawaiian *Metrosideros* Forest Mortality Using Laser-Guided Imaging Spectroscopy

Nicholas R. Vaughn ^{1,*} , Gregory P. Asner ¹ , Philip G. Brodrick ¹ , Roberta E. Martin ¹ ,
Joseph W. Heckler ¹, David E. Knapp ¹ and R. Flint Hughes ²

¹ Department of Global Ecology, Carnegie Institution for Science, Stanford, CA 94305, USA; gpa@carnegiescience.edu (G.P.A.); pbrodrick@carnegiescience.edu (P.G.B.); rmartin@carnegiescience.edu (R.E.M.); jheckler@carnegiescience.edu (J.W.H.); dknapp@carnegiescience.edu (D.E.K.)

² Institute for Pacific Islands Forestry, Pacific Southwest Research Station, USDA Forest Service, 60 Nowelo St, Hilo, HI 96720, USA; fhughes@fs.fed.us

* Correspondence: nvaughn@carnegiescience.edu; Tel.: +1-650-843-9073

Received: 2 February 2018; Accepted: 20 March 2018; Published: 22 March 2018



Abstract: Rapid ‘Ōhi‘a Death (ROD) is a disease aggressively killing large numbers of *Metrosideros polymorpha* (‘ōhi‘a), a native keystone tree species on Hawaii Island. This loss threatens to deeply alter the biological make-up of this unique island ecosystem. Spatially explicit information about the present and past advancement of the disease is essential for its containment; yet, currently such data are severely lacking. To this end, we used the Carnegie Airborne Observatory to collect Laser-Guided Imaging Spectroscopy data and high-resolution digital imagery across >500,000 ha of Hawaii Island in June–July 2017. We then developed a method to map individual tree crowns matching the symptoms of both active (brown; desiccated ‘ōhi‘a crowns) and past (leafless tree crowns) ROD infection using an ensemble of two distinct machine learning approaches. Employing a very conservative classification scheme for minimizing false-positives, model sensitivity rates were 86.9 and 82.5, and precision rates were 97.4 and 95.3 for browning and leafless crowns, respectively. Across the island of Hawaii, we found 43,134 individual crowns suspected of exhibiting the active (browning) stage of ROD infection. Hotspots of potential ROD infection are apparent in the maps. The peninsula on the eastern side of Hawaii known as the Puna district, where the ROD outbreak likely originated, contained a particularly high density of brown crown detections. In comparison, leafless crown detections were much more numerous (547,666 detected leafless crowns in total) and more dispersed across the island. Mapped hotspots of likely ROD incidence across the island will enable scientists, administrators, and land managers to better understand both where and how ROD spreads and how to apply limited resources to limiting this spread.

Keywords: biological invasion; Carnegie Airborne Observatory; forest pathogens; Hawaii Island; Rapid ‘Ōhi‘a Death

1. Introduction

Despite its tropical latitude, the island of Hawaii has relatively low plant diversity due to its age and isolation. A large share of the species in the Hawaiian Islands have evolved in the region and are therefore unique to the archipelago. One of these endemic species, *Metrosideros polymorpha* (‘ōhi‘a), is the most prevalent tree on Hawaii Island. Likely due to its high degree of evolved polymorphism [1,2], ‘ōhi‘a is present as a dominant or co-dominant tree in all the forested ecological zones on the island ranging from sea level to 2700 m above sea level, occupying an area larger than

250,000 ha [3]. ‘Ōhi‘a accounts for more than 50% of the total basal area of woody plants throughout the Hawaiian archipelago [4]. As such, this species supports a large number of associated endemic plant and animal communities found on the island [3,5], and it is deeply engrained into Hawaiian culture [3]. Substantial losses of this keystone species would fundamentally and permanently change the ecological and cultural landscape of the island [4,6,7].

In 2010, a large number of ‘ōhi‘a trees began exhibiting browning foliage, rapidly followed by tree mortality. In subsequent years, the incidence of ‘ōhi‘a canopy browning and mortality spread dramatically, affecting an area of more than 20,000 hectares by late 2016 [8]. In response, a multi-agency team of scientists, forest managers, and concerned citizens assembled to determine the cause and review approaches to fight the spread of this disease, subsequently named Rapid ‘Ōhi‘a Death (ROD). Two distinct and previously unknown fungal species in the genus *Ceratocystis* were eventually isolated as the pathogens causing ROD [9]. In recent years, hundreds of confirmed cases of ROD resulting from at least one of two *Ceratocystis* species have been documented in ‘ōhi‘a stands across the island. Infection by either of these two pathogens causes a similar progression of symptoms, although at a slightly different pace. The infection is first noticeable when leaves on one or more branches of the tree begin to yellow, wilt, and turn brown within days to weeks. This brown stage is quite noticeable, and it is relatively unique to ROD infection [10] (this issue). Brown leaves then drop from the infected tree over several weeks to months until only bare branches remain.

While the cause and progression of the disease in individual ‘ōhi‘a are fairly well understood, many important questions remain with respect to how the disease spreads and how to slow down this spread. Knowledge of the full extent of ROD infection across the island, both current and past, is critical to the determination of how and where to apply limited resources to contain the disease. However, because of the span of spatial scale involved—‘ōhi‘a crowns are relatively small, and infections are scattered across an area of many thousands of hectares of remote forest—detection of ROD-infected trees across the island remains a challenge. Currently available tools fall short in accomplishing this task [8]. In addition, the most extensive ‘ōhi‘a forests lie in very remote areas and on private property, making them difficult to reach on foot. Unmanned aerial vehicles are quick to deploy and offer very high-resolution, detailed imagery, but are only able to map small areas at a time and are not permitted over certain federal and most private land. The efficacy and coverage of helicopter surveys is limited by the ability of the human eye to spot single brown crowns at a distance, by a lack of spatial accuracy, and by the substantial cost of flight time. Conversely, data from Earth-orbiting satellites are readily available and could cover the full region, but are too spatially or spectrally coarse to pinpoint individual browning trees. These shortcomings suggest that appropriate mapping data collected from higher-altitude aircraft may be able to provide the needed coverage and resolution to identify potential ROD infections across the island.

The Carnegie Airborne Observatory (CAO) [11] is uniquely able to fill this gap, as it is able to collect laser-guided imaging spectroscopy (LGIS) data from altitudes of 2000 or more meters above ground level. LGIS is the fusion of data from a high-fidelity visible-to-shortwave imaging spectrometer (VSWIR) to three-dimensional information provided by a light detection and ranging (LiDAR) scanner [12,13]. This combination of boresight-aligned instruments allows spectrometer readings from a forest canopy to be mapped to sub-meter precision. Asner et al. [10] (in review) demonstrate that various stages of ROD infection exhibit distinct LGIS spectra at leaf to canopy scales, and they used this information to develop a spectral mapping signature for ‘ōhi‘a trees likely infected by ROD. Here, we show that those LGIS spectra can be used to produce maps of both current ROD infections (i.e., brown, desiccated ‘ōhi‘a tree crowns) and past ROD infections (i.e., fully-dead, leafless tree crowns). We apply the LGIS approach to map brown and leafless ‘ōhi‘a trees throughout Hawaii Island in 2017, and we assess its accuracy for future mapping efforts with the intent to track the spread of the disease in space and time.

2. Materials and Methods

2.1. Airborne Data Collection

We collected data with the CAO between 7 June and 5 July 2017 over the island of Hawaii with three co-aligned instruments: a visible-to-shortwave imaging spectrometer (VSWIR), a dual-channel airborne light-detection and ranging (LiDAR) scanner, and a high-resolution 3-band (red, green, and blue) 60-megapixel digital camera. For optimal flight coverage, the island was partitioned into 15 compartments of fairly uniform forest type ranging in size from 12,000 to 75,000 ha. During flight, aircraft speed was maintained within 10% of the 60 m s⁻¹ nominal air speed and within 200 m of the nominal planned elevation of 2000 m above ground level. The LiDAR was operated at an effective pulse frequency of 200 kHz, a scan frequency of 34 Hz, 30 percent overlap, and total field-of-view of 38 degrees to match the 34-degree FOV of the VSWIR after clipping 2 degrees from the scan edges. These settings yielded a mean density of 3.3 pulses m⁻² and a VSWIR resolution of 2 m. VSWIR data were collected in 427 channels between 350 and 2485 nm at 5 nm increments (full-width at half max). The high-resolution digital camera had an effective resolution of 24 cm.

2.2. Data Processing and Orthorectification

Estimated location error in LiDAR point vertical positioning from planar surface analysis was less than 10 cm (root mean squared error). LiDAR point cloud data were processed to 1-m resolution digital surface maps of ground elevation, canopy surface elevation, and canopy surface height above ground using the LAStools software suite (Rapidlasso GmbH; Gilching, Germany).

The VSWIR radiance data were first orthorectified using LiDAR surface maps, position, and orientation data from the on-board GPS-IMU navigation system, and known boresight and position offsets between the two instruments. To improve the signal-to-noise ratio, the radiance data were reduced by averaging each pair neighboring bands. This yielded a dataset of 214 bands at increments of 10 nm. Using computed observation angles and elevation, atmospheric correction was performed using ACORN-6LX software (Imspec LLC; Palmdale, CA, USA) to transform the VSWIR radiance data into surface-level reflection spectra. For each flight line, we used an iterative procedure to find the optimal setting for the ACORN-6LX visibility parameter that is used to specify the amount of aerosols present at the time of collection. Beginning with a setting of 100 km, the visibility parameter was decreased until the resulting reflectance at 420 nm was <1%. The individual VSWIR reflectance data were mosaicked into one image for each of the 15 flight coverage compartments using the criteria of minimum phase angle (angle from sun to target to instrument) for overlap regions. These coverages were mosaicked into a full island map using the criteria of maximum normalized difference vegetation index (NDVI).

2.3. Training Data

Using orthorectified color images from the on-board digital camera as a reference, we identified 688 VSWIR pixels within crowns exhibiting the brown state of ROD infection, labeled “Brown”, and 903 VSWIR pixels within leafless crowns, labeled “Leafless”, across the entirety of ‘ōhi‘a stand distribution on Hawaii Island (Figure 1). Because signal from background vegetation can have a large impact on observed spectra, especially in leafless crowns, care was taken to select training pixels from central regions of crowns and that tree branching was dense enough to ensure that the resulting spectra would be dominated by the class of interest. We also identified 13,946 pixels representing other entities we were not interested in mapping; these were primarily living canopies of other plant species, along with a small number of non-vegetation targets such as bare ground, manmade structures, and other surfaces, all of which provided the model with a third target class, labeled “Live”. The non-vegetated pixels make up <1% of the target set; therefore, despite their spectral characteristics being different from each other and living vegetation, we chose to include them in the living category, because we were not interested in separating samples classified into this category. A few shaded pixels

were included for each of the three classes to reduce any artifact caused by decreased signal-to-noise ratios in darker pixels.

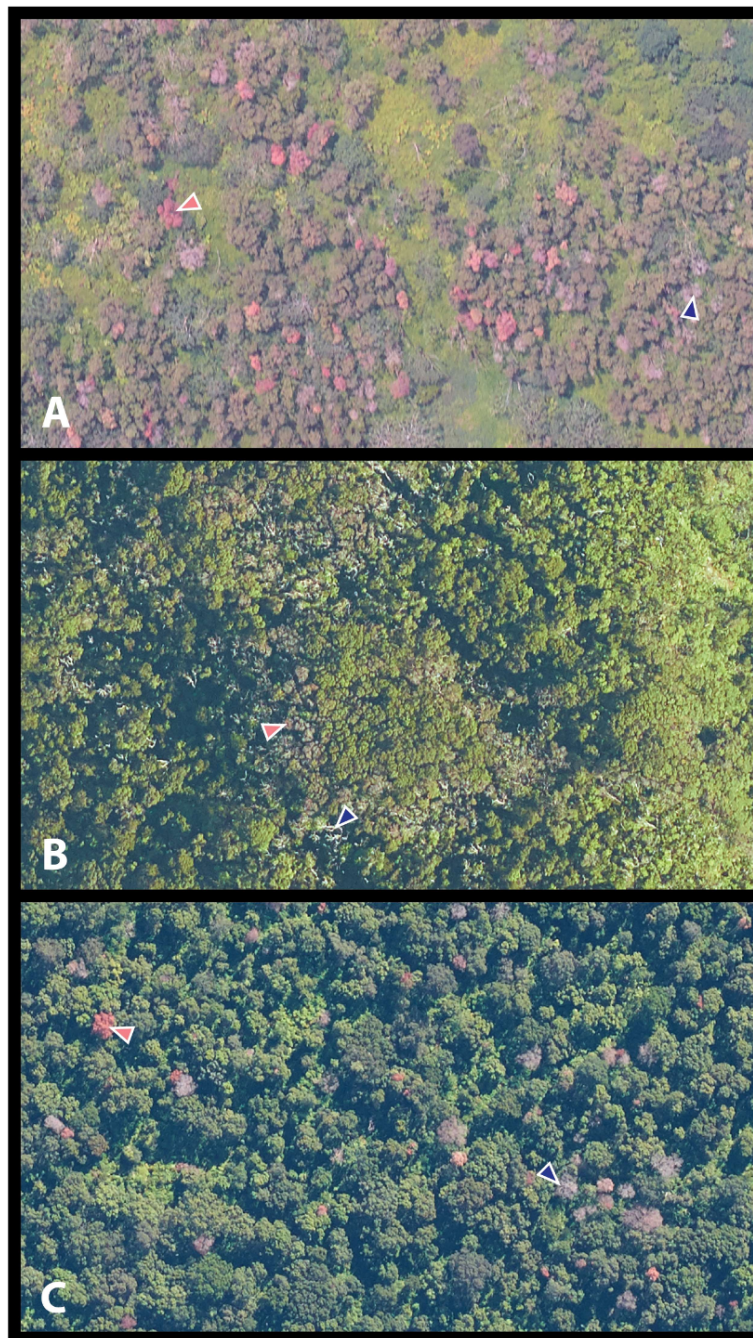


Figure 1. Example images from the Carnegie Airborne Observatory high-resolution digital camera showing suspected ROD-infected brown-state crowns along with nearby leafless crowns. Such regions were used as training and validation data. Scenes are from the regions of Puna (A), Kohala (B), and Kona (C). Light red arrows point to example brown-state trees and dark blue arrows point to example leafless trees.

The full VSWIR reflectance spectrum was extracted for each of these training pixels and labeled by class (Figure 2). Reflectance values of wavelengths known to be absorbed or scattered by atmospheric constituents were removed, leaving 159 bands representing four regions of the measured spectrum

(Table 1). Cleaned individual spectra were subsequently brightness-normalized (BN), such that the magnitude (Euclidean norm) of each BN spectrum was 1.0. This was done for each spectrum (pixel) using the formula

$$\vec{v}_n = \frac{\vec{v}_r}{\|\vec{v}_r\|}, \quad (1)$$

in which \vec{v}_r is the original reflectance spectrum as a vector, \vec{v}_n is the brightness-normalized reflectance spectrum.

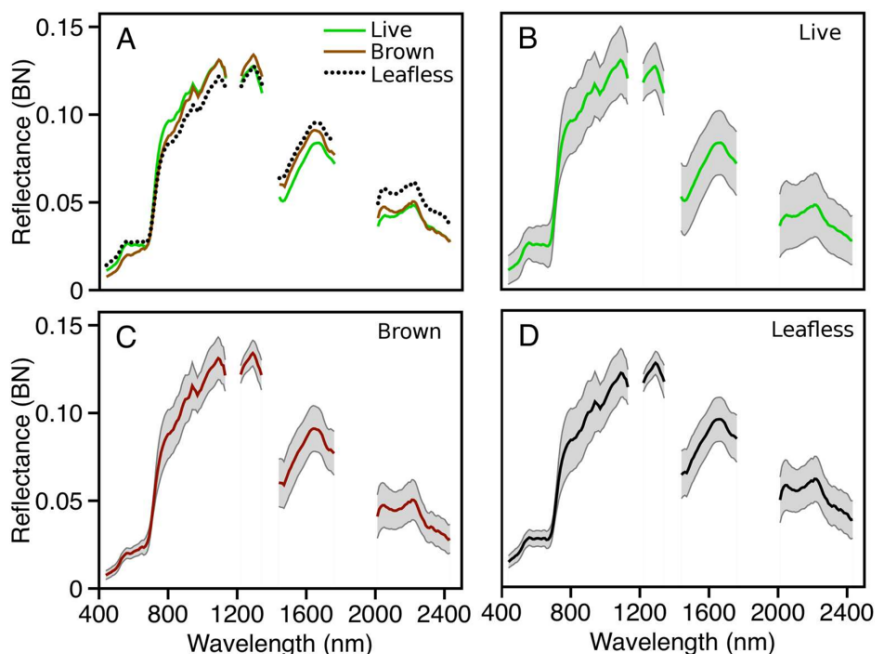


Figure 2. Mean, brightness-normalized spectra for 15,537 training points in the *Live*, *Brown*, and *Leafless* classes (A). The *Live* (B), *Brown* (C), and *Leafless* (D) mean spectra are also shown with their associated band standard deviation windows in grey. These distinct spectra show the degree of separation between the different classes.

Table 1. CAO VSWIR wavelengths used in the classification models.

Group	Number of Bands	Beginning Wavelength (nm)	Ending Wavelength (nm)
VIS-NIR	70	439.26	1030.29
IR	13	1220.43	1340.60
SWIR1	33	1440.76	1761.23
SWIR2	43	2011.60	2432.23

2.4. Modelling

Both false detections and false omissions have the potential to waste resources when final maps are used in the field; we sought to maximize the model results under dual criteria of high sensitivity and high precision. To meet this goal, we combined two model forms into an ensemble model for differentiating pixels within the *Brown* and *Leafless* classes from those in the *Live* class. The first model form was a Support Vector Machine (SVM), which finds optimal divisions between the data points in n-dimensional vector space [14]. This machine learning tool has been demonstrated to be an effective classification tool with hyperspectral data [15,16] and has performed well with CAO data in particular [17–19]. SVMs naturally incorporate information from all wavelengths of each input spectrum and offer the benefit of being computationally simple to train and apply. The second model

form used was the Gradient Boosting Machine (GBM) [20,21]. GBM models are created by generating an ensemble of fairly weak (shallow) decision trees. Because each successive tree is fit to the remaining residuals from the previous combination of trees, a process known as ‘boosting’, GBMs incorporate both bias and variance reduction, distinguishing them from other decision-tree based approaches such as a Random Forest (RF), which are focused on variance reduction. GBM models are able to incorporate nonlinear interactions between spectral features while also being robust to spectral collinearity. We found GBM models outperformed RF models during exploratory testing in this study.

We found optimal model parameters for both the SVM and GBM fits using a multi-stage grid search technique. The first stage grid covered a broadest region of the available parameter space with the intent of surrounding the most-optimal parameters. The search grid for each successive stage used finer granularity, covering a small region of the grid that proved most optimal in the last stage. A 10-fold cross-validation was performed for each set of parameters in the grid to get a reasonable estimate of how well the model would perform on new data. All model training was done using the package scikit-learn [22] for Python. As the same tree canopy can simultaneously contain both brown foliage and leafless branches, leaving the canopy state rather ambiguous, we focused less on misclassifications between these two states and more on misclassified living trees. In addition, errors of commission regarding living trees would be much more problematic to users of the final maps. Thus, the criteria used during model parameter selection for both models was the number of correctly classified *Brown* and *Leafless* pixels (combined) while holding the false positive rate of each of the *Brown* and *Leafless* classes to less than 1% (independently). Error rates were assessed on a per-pixel, rather than a per-crown, basis because of the relatively large number of small, single-pixel instances in the training data. Once optimal parameter values for each model were obtained, we trained final models with the full set of training pixels using these parameters to build models for subsequent full-island map application.

We next devised a way to combine the two models in order to improve the applied model predictions. Both models, when applied at the whole-island scale, left patches of false-positives for either the *Brown* or *Leafless* classes due to heavily site-specific vegetation or observation conditions. We sought to eliminate these artifacts, while preserving model accuracy. Initial testing suggested that the SVM model was better at detecting *Brown* and *Leafless* pixels yet more prone to false positives. We found that the best performance with the least amount of artifact occurred when the GBM model was able to ‘veto’ perceived spurious predictions of the SVM. For each pixel and for each class, each of the two models produced a likelihood value between 0 and 1, which effectively portrays the model’s confidence that a given pixel belongs to a given class. We found that the vast majority of false positives in maps produced by the SVM model had only moderate likelihood values, yet corresponding likelihood values from the GBM model were extremely low. Using this feature to our advantage, any SVM likelihood value for *Brown* or *Leafless* classes of less than 0.975 was replaced by the associated GBM likelihood, if the GBM likelihood value was less than 0.01. For a given class i , this model combination rule can be written as

$$L_i = \begin{cases} L_{i,gbm} & \text{if } L_{i,svm} < 0.975 \text{ and } L_{i,gbm} < 0.01, \\ L_{i,svm} & \text{otherwise,} \end{cases}$$

in which L_i is the combined model likelihood value for class $i \in \{Brown, Leafless\}$, $L_{i,svm}$ is the SVM model likelihood value for class i , and $L_{i,gbm}$ is the GBM model likelihood value for class i . For the likelihood values produced by the above combination approach, still in the range 0 to 1, we used the following decision rule to assign a class to each pixel:

$$C(T, L_V, L_B, L_D) = \begin{cases} \text{Live} & \text{if } L_B < T \text{ and } L_D < T, \\ \text{Brown} & \text{if } L_B \geq T \text{ and } L_D \geq T \\ \text{Leafless} & \text{otherwise,} \end{cases}$$

in which L_V , L_B , and L_D are likelihood values for classes *Live*, *Brown*, and *Leafless*, respectively, T is a specified likelihood threshold value, and C is the predicted classification of a given pixel.

2.5. Model Application

We used a combination of two metrics to evaluate potential values of the likelihood threshold value, T , for application of the combined model to full maps of Hawaii Island. For a given value of T , we computed classification sensitivity (producer accuracy) and classification precision (user accuracy) for the *Brown* and *Leafless* classes using the SVM, GBM, and combined model predictions from the 10-fold cross-validation training under the optimal parameters for each model. We repeated this calculation for each of 19 values, $T \in \{0.05, 0.10, \dots, 0.95\}$, to produce response curves of both metrics for both *Brown* and *Leafless* classes.

Ultimately, we selected threshold of 0.65, with which we applied the combined model decision rule $C(T, L_V, L_B, L_D)$ to the model prediction likelihood values of the full CAO VSWIR coverage of the island. Because VSWIR pixels are 4 m^2 in area, light reflecting from brown vegetation on the ground can blend with light reflecting from the edges of tree vegetation, causing the spectra for a number of edge pixels to be identified as *Brown* or *Leafless*. We filtered out false detections due to such edges by using the canopy height data built from the LiDAR data. If the LiDAR-derived height of the top of the vegetation surface was $<1.5 \text{ m}$ in any of the four $1 \text{ m} \times 1 \text{ m}$ quadrant subregions within a VSWIR pixel, then the pixel was re-classified as *Live* when building output maps.

2.6. Additional Spectral Filtering

Field verification of early versions of the final map indicated that excessive false-positives remained for the *Brown* class. There were three scenarios in which a crown in the map was not observed to be a leafless 'ōhi'a in the field later in the same year. Each of these scenarios below involved vegetation not represented in the training data sets.

1. A small number of instances of crowns in the far north region, Kohala, were classified as *Brown* but observed to be green three months after the CAO flight coverage. The most likely cause of this was that these were 'ōhi'a exhibiting unusually heavy flowering ('ōhi'a flowers are typically bright red) along with relatively low foliage. This situation may have been exacerbated by an extremely low sun angle at the time of overflight.
2. In the region of Hawaii Volcanoes National Parks, some instances of tall or climbing brown *Dicranopteris linearis* fern (uluhe) were found to be misclassified as *Brown* by the model.
3. Also in the region of Hawaii Volcanoes National Park, a large number *Morella faya* (firetree) trees are known to be dying in the area. These trees also appear dry and brown—similar, but not identical, to 'ōhi'a in the brown-state of ROD infection—and the model classified map pixels, covering them as *Brown* with high likelihood values.

We created a filter to reduce detected crowns under these false-positive scenarios using an analysis of the spectra of the affected pixels. The pixels from brown *D. linearis* fern and flowering 'ōhi'a in scenarios 1 and 2 all had highly-negative slopes in the red-green region of the visible spectrum (600–680 nm), whereas brown 'ōhi'a and *M. faya* both consistently had positive slopes in the same spectral region. We therefore used the following criteria to identify and remove such pixels from the map.

$$(r_{650} + r_{660}) - (r_{600} + r_{610}) < -0.004 \quad (2)$$

in which r_w is the reflectance at the indicated wavelength w in nm. *M. faya* pixels classified as *Brown* (scenario 3 above) were separable from verified *Brown* 'ōhi'a pixels using a combination of two features: (1) the peak height difference between the infrared and first shortwave regions of the spectrum was

greater for 'ōhi'a pixels and (2) the slope of the peak in the first shortwave region (1640–1680 nm). We employed the following criteria to identify and remove brown *M. faya* pixels from the map.

$$r_{1290} - r_{1650} \leq 0.0396 \quad (3)$$

While we do not believe any examples of brown *D. linearis* fern, brown *M. faya*, or flowering 'ōhi'a were represented in the training data, some of the *Brown* training pixels were caught by one or more of the two spectral filter criteria. For the purposes of evaluating map accuracy, it was unclear how to represent these ambiguous pixels in a confusion matrix. Applying the filter criteria to just the predicted classes would show degraded mapping performance over the pre-filter results, while applying the filter criteria to both observed and predicted classes would show improvement. We therefore simply kept track of the number of pixels affected, and performed an analysis of the potential effects of this filtering on model sensitivity of *Brown* pixels.

We made final maps of the locations of suspected ROD-infected brown 'ōhi'a tree crowns (as clusters of predicted *Brown* pixels) and leafless tree crowns (as clusters of predicted *Leafless* pixels) from the remaining pixel-level detections. Centroid points of all contiguous, adjacent (no diagonal connections) clusters of *Brown* or *Leafless* pixels greater than or equal to two pixels (8 m²) in size were used as spatial coordinates for suspected brown-state 'ōhi'a or leafless tree crowns. Although only a small number of points were found in areas known to not contain 'ōhi'a, these points were considered false detections and were therefore masked out in the final maps.

3. Results

We found both the SVM and GBM models to be capable of detecting a high number of *Brown* and *Leafless* training pixels with minimal false detection. Use of a radial basis function (RBF) for the SVM model yielded the best results. Under this kernel, the optimal parameter values were a gamma of 0.0075 and cost of 200. For the GBM approach, optimal parameter values were a learning rate of 0.225, a maximum tree depth of 6, and the assembly of 1750 trees.

Cross validation results indicated that the SVM was more sensitive to spectral features that define both *Brown* and *Leafless* classes (Table 2). Sensitivity values were 90.1% and 88.0% for *Brown* and *Leafless* classes, respectively. The sensitivity rate for both these classes combined, compared to the *Live* class, was 90.5%. GBM was considerably more conservative during training, with many more false-negatives for the *Brown* class, though it seemed to be slightly better at distinguishing *Brown* from *Leafless* pixels. The GBM *Brown* sensitivity was 70.8%, *Leafless* sensitivity was 65.1%, and combined *Brown* and *Leafless* sensitivity was 69.5%. Upon application, the SVM was much more prone to erroneous detections of both *Brown* and *Leafless* pixels due to lighting or forest canopy conditions not represented in the training dataset.

Table 2. Confusion matrix results from the cross-validation procedure of the optimal fit of the Support Vector Machine (SVM) model and Gradient-Boosted Machine (GBM) model. Here a likelihood value threshold of 0.5 was used for each model.

Observed	Predicted					
	SVM <i>Live</i>	SVM <i>Brown</i>	SVM <i>Leafless</i>	GBM <i>Live</i>	GBM <i>Brown</i>	GBM <i>Leafless</i>
<i>Live</i>	13,877	13	56	13,869	29	48
<i>Brown</i>	61	620	7	198	487	3
<i>Leafless</i>	96	12	795	307	8	588

When analyzing the effect of threshold value on the different models, we found a generally slow decline in true detection rates for all models as the likelihood threshold *T* increased from 0 to approximately 0.8 (Figure 3). Thus, selection of any value within this range will still result in a high number of true positives. Additionally, the rate of decline was significantly lower for the GBM model

compared to the SVM model. This analysis showed that the combined model retained nearly all of the superior sensitivity of the SVM model, indicating that for most of the truly *Brown* or truly *Leafless* training pixels the GBM was in at least partial agreement.

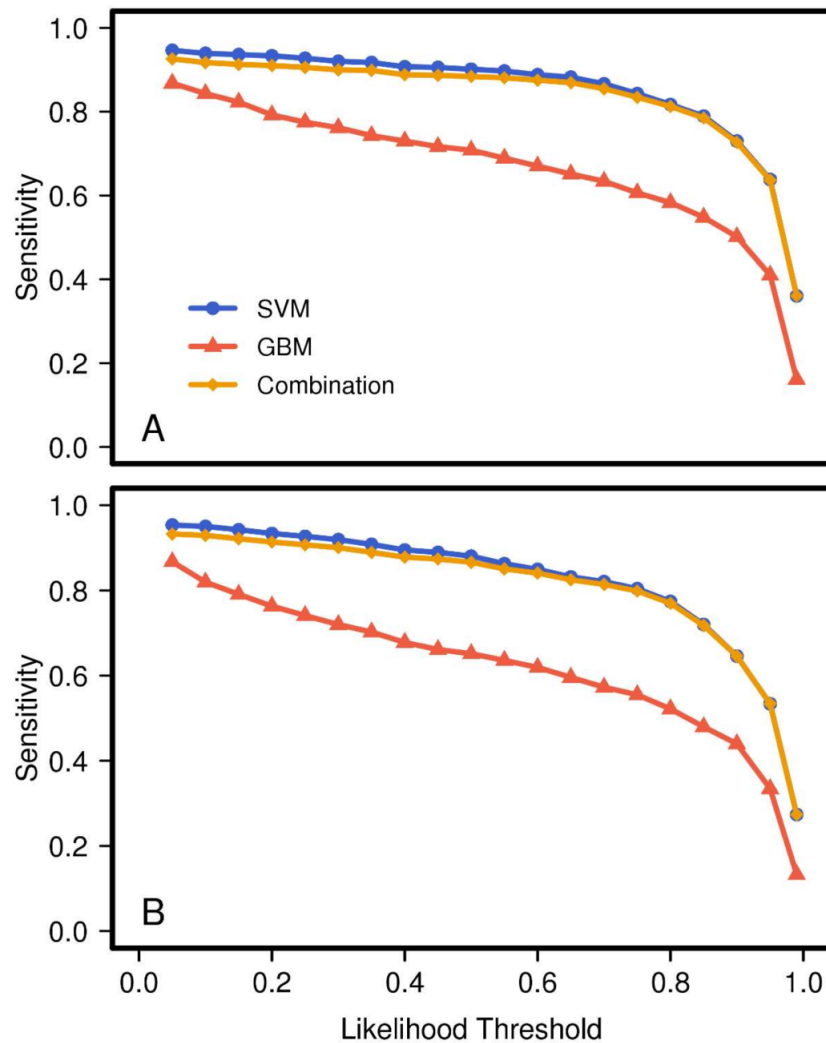


Figure 3. Effect of likelihood threshold selection on the proportion of training pixels from of a given class predicted to belong to the correct class (sensitivity) for both *Brown* (A) and *Leafless* (B) observed pixel classes, under the SVM, GBM, and combined models using a 10-fold cross-validation.

Similarly, precision rapidly increased with T to >90% for all models in the range 0 to ca. 0.4 (Figure 4). However, compared to the values for sensitivity, the difference between models was not as large. The rate of precision for *Brown* pixels was lower for the GBM than for the SVM. However, with respect to *Leafless* pixels, the two models had nearly the same values for precision. We found the combined model not only kept the properties of the best of its component models, it improved upon them. Here, the combined model *Brown* pixel precision values most rapidly improve with increasing threshold, reaching a semi-plateau by a threshold value of 0.2. To a lesser degree the same was true for *Leafless* pixels.

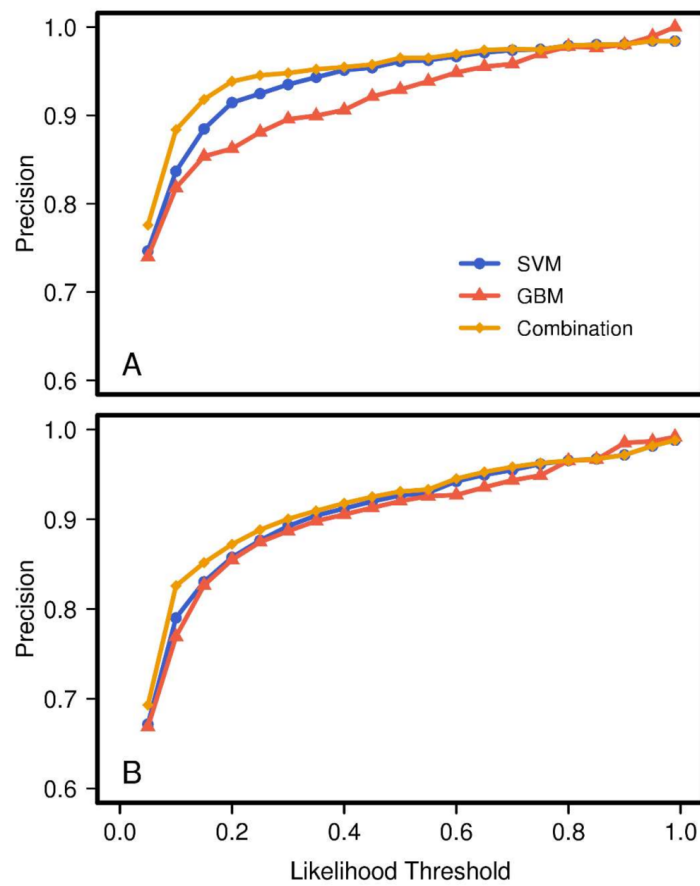


Figure 4. Effect of likelihood threshold selection on the proportion of training pixels of a given predicted class that truly belong to the class (precision) for both *Brown* (A) and *Leafless* (B) predicted pixel classes, under the SVM, GBM, and combined models using a 10-fold cross-validation.

Given the above results, and upon inspection of several sample map areas, we selected a likelihood threshold of 0.65. When applied to the combined model, this threshold maintained desirable detection rates (i.e., sensitivity values of 86.9% and 82.5% for *Brown* and *Leafless* pixels, respectively), while greatly reducing the false positives (i.e., precision values >95% for both classes) to acceptable levels (Table 3). The kappa statistic for this classification was 0.895. Only 42 of the 13,946 *Live* training samples were misclassified as class *Brown* or *Leafless*, indicating the model is more likely to classify ambiguous trees as *Live*.

Table 3. Confusion matrix of the cross-validation procedure for the chosen value of likelihood threshold ($T = 0.65$) for the decision rule on the combined model.

Observed	Predicted			Sensitivity (%)
	<i>Live</i>	<i>Brown</i>	<i>Leafless</i>	
<i>Live</i>	13,904 (89.5%)	6 (0.0%)	36 (0.2%)	99.7
<i>Brown</i>	89 (0.6%)	598 (3.8%)	1 (0.0%)	86.9
<i>Leafless</i>	148 (1.0%)	10 (0.1%)	745 (4.8%)	82.5
Total				98.1
Precision (%)	98.3	97.4	95.3	
Specificity (%)	97.0	99.4	98.9	

The spectral filtering to remove *D. linearis* fern, *M. faya* tree, and flowering 'ōhi'a affected a noticeable number of *Brown* training pixels. We found that 48 of the 688 *Brown* training pixels met the

criteria for one or both of the two spectral filters (Equations (1) and (2)). Thus, assuming our training pixels truly contain no examples of *D. linearis* fern, *M. faya* tree, or flowering 'ōhi'a, the model may lose up to 7.0% of *Brown* pixel sensitivity by applying these filters. However, 19 of these 48 pixels were not even identified as *Brown* by the combined model before filtering, indicating the actual loss in sensitivity might be closer to 4.2%. Of the 8316 *Live* pixels that met one or more of the filter criteria, none were mistakenly classified as *Brown*. This indicates that, outside the region of Hawaii Volcanoes National Park, this particular type of misclassification is probably rare.

The LiDAR-derived canopy height and the spectral filtering both reduced the number of isolated *Brown* pixel detections, resulting in a statistically robust map with very little visual artifact present (Figure 5). Across the island of Hawaii, we found 43,134 individual crowns suspected of exhibiting the brown state of ROD infection. Hotspots of potential ROD infection are apparent in the maps. The peninsula on the eastern side of Hawaii known as the Puna district, where the ROD outbreak likely originated, contained a very high density of brown-state crown detections.

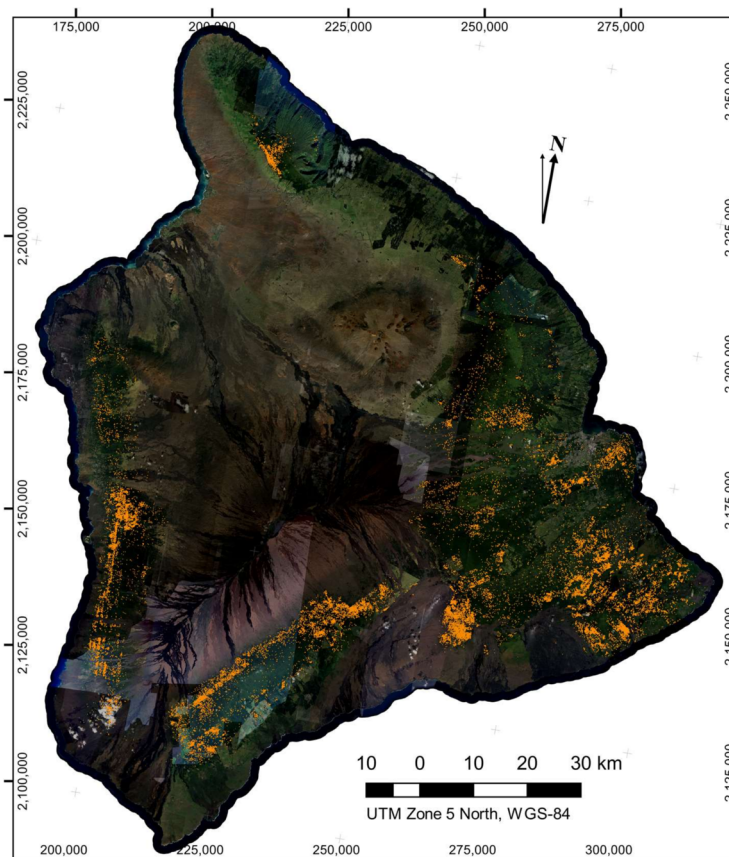


Figure 5. Map of the brown-state 'ōhi'a crowns detected using our modeling and filtering approach applied to the CAO coverage of Hawaii in June 2017. Individual points represent single detections of 8 m² or greater. For visibility, individual points are 120 m in diameter at this map scale. Therefore, denser clusters of detected crowns appear as contiguous regions on the map. Background imagery from Google, DigitalGlobe (2017).

In comparison, leafless crown detections were much more numerous (547,666 detected leafless crowns in total) and more dispersed across the island (Figure 6). It was apparent in the map (Figure 6) that detection of leafless crowns was more sensitive to cross-flightline observation angle effects, leading to some linear artifact in the maps. However, we saw no evidence of an increase in false-positive rates of leafless crowns due to these viewing angle effect, but rather we observed that a decrease in detection on one side of each flightline was the cause of the artifacts. As viewing angle and solar

angles approach nadir, green undergrowth beneath a thin, leafless crown has a more dominant effect on reflectance, leading to this decreased detection. Since we were unable to distinguish the cause of death for so many trees, we cannot ascertain what percentage of leafless crowns were the result of ROD. However, dense areas of detected leafless crowns can be found in regions containing higher counts of brown-state crown detections, and ROD is expected to be the dominant cause of death in these locations.

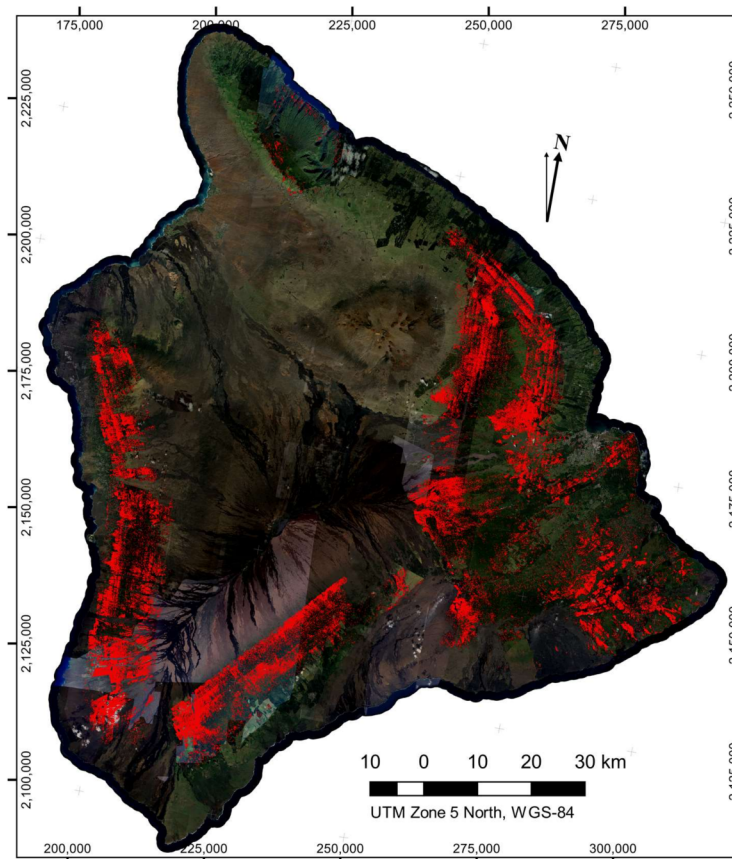


Figure 6. Map of the leafless tree crowns detected using our modeling and filtering approach applied to the CAO coverage of Hawaii in June 2017. Individual points represent single detections of 8 m² or greater. For visibility, individual points are 50 m in diameter at this map scale. Therefore, denser clusters of detected crowns appear as contiguous regions on the map. Background imagery from Google, DigitalGlobe (2017).

4. Discussion

Using CAO laser-guided imaging spectroscopy, we obtained very high classification accuracy for detecting brown-state, potential ROD-infected, and leafless trees with both the GBM and SVM models and their combination. This suggests that the spectra of these two classes were highly distinguishable from surrounding vegetation. While it was possible to visually identify particular brown and leafless crowns with certainty in the three-band (red, green, and blue) 24 cm aerial imagery due to the location and pattern of occurrence, this was not the case for all images captured across the island. Due to differences in lighting conditions and aircraft movement, our RGB imagery was insufficient to determine whether some trees were truly exhibiting the brown state of ROD infection. This is why hyperspectral data are often sought for difficult classification problems [7,23,24]. As their canopies turn brown, ROD-infected 'ōhi'a trees also experience a characteristic change in leaf chemical composition and shape, both of which highly affect the reflection of light across the full spectrum measurable by imaging spectroscopy [25] (Figure 2).

The ensemble approach of mixing two model forms greatly improved whole-island brown-state and leafless detection maps. SVM models have been used extensively in remote sensing classification applications [16], and GBM models have more recently shown promise in the field [18,26,27]. Yet, individually, each of the two model forms was prone to misclassification when applied to regions of the island not represented in the training data. An increase in training data would likely help address this issue, but generating a training set that completely spans the extremely diverse climate and biogeographical conditions represented on the island of Hawaii [28,29] presents a major challenge. Fortunately, each model form was overactive in different parts of the island and under different conditions. We were able to take advantage of this effect by combining the models into an ensemble. Ensemble models in general have been shown to improve performance over individual component models [30–32]. In fact, a GBM itself is a form of ensemble modeling, as classification trees are sequentially added during boosting to incrementally improve fit [33]. Additionally, more diversity in the component models of an ensemble has been shown to improve ensemble model performance and further reduce overfitting [34]. Here, we mixed two distinct model forms and were able to reduce overfitting (manifested most-critically as artifacts in the final maps) while retaining high target detection capabilities.

The range of spatial scale of this project was extreme in the sense of applied geospatial classification models. VSWIR data collected by the CAO in 2017 covered an area of approximately 525,000 ha, about 320,000 ha of which is considered forested. This suggests that our maps cover nearly 800 million pixels potentially able to contain infected 'ōhi'a. There are few examples of classification maps covering such a large area at high spatial resolution. This is not surprising given the challenges encountered in such a project. In addition to the challenging problem of minimizing flight coverage costs subject to unpredictable tropical weather conditions, merging data from numerous flights occurring under diverse lighting conditions is quite difficult. The boundary between two different collections can easily result in visible artifacts in maps [35,36]. Neighboring areas may be covered by flight lines collected under extremely different conditions. Additionally, effects of the bi-directional reflectance distribution function (BRDF) may significantly alter the shape of recorded spectra [37] and affect model predictions, although the “pushbroom” style of collection of the VSWIR instrument essentially keeps this a cross-track problem. In this project we chose to handle these challenges with a custom flight line mosaic scheme, manual cloud masking, and most importantly, training data identification across regions of diverse lighting and view angle conditions. While not entirely free of viewing angle artifact (see Figures 5 and 6), the resulting maps of the crown classes of interest, with surprisingly little artifact, across nearly a full month of data collection.

We chose a pixel-based approach for mapping brown and leafless trees, primarily because our target of interest was partial crowns. ROD symptoms typically spread from whole branch to whole branch [8]; as such, we believed a focus on pixel-sized was essential to keep model sensitivity high and consistent across the landscape. Working at the crown level was an alternative approach to this problem, and there are several tools available for the automatic delineation of individual tree crowns from LiDAR data [38–40], but had we incorporated this methodology, there would have been several setbacks. First, these tools are most-often used for small regions of fairly simple, consistent vegetation growthform (e.g., boreal forest). In contrast, the variation in growthform among living 'ōhi'a across Hawaii Island is incredibly high. Adding more variation from dead or dying trees would only increase this complexity. In addition, there are many instances of multiple tree crowns blending together into a single uniform canopy, which severely limits the efficacy of individual crown segmentation [38,39].

Our resulting maps detailing the extent and distribution of both brown-state crowns and leafless crowns across broad regions of Hawaii Island reveal a startling extent of mortality. The extent and distribution of brown-state canopies presented here agree well with Hawaii Island-wide helicopter surveys conducted in January 2017 that estimated that ca. 30,000 ha of 'ōhi'a forest stands had recently experienced levels of *Ceratocystis*-induced mortality >10% (unpublished data, Hawaii Department of Land and Natural Resources). Although approximately half a million leafless crowns documented

across Hawaii Island cannot and should not be uniformly attributed to *Ceratocystis*-induced Rapid 'Ōhi'a Death (ROD), it is likely that the majority of the 43,134 trees exhibiting brown canopies in our 2017 imagery were experiencing the lethal effects of such *Ceratocystis* infection. Furthermore, these brown-state canopies constitute relatively recent mortality, certainly within the last year, and likely within 6 months prior to image collection. We employed numerous measures to reduce false-positive detection rates, such as a high likelihood threshold of 0.65 for class inclusion and minimum cluster size of 8 m². These measures likely affect small trees more than large trees. However, this may not be a large problem, because prior results suggest that medium-sized trees are the most affected by ROD [8]. In addition, instances of isolated small brown-state trees should be minimal, because the disease spreads so quickly [9]. If small individual crowns were not detected, we feel it is very likely that many infected crowns in the surrounding area were detected, and final maps should accurately reflect the relative density of ROD infection.

A prior, well-acknowledged, and well-studied process of 'ōhi'a mortality characterized as "'ōhi'a dieback" was responsible for high levels of mortality across an estimated 50,000 ha of windward portions of Hawaii Island during the thirty years between the mid-1950's to the mid-1980's [41]. By comparison, *Ceratocystis*-induced ROD has affected more than half that amount of area (i.e., 30,000 ha) in approximately one-tenth the time. Our brown-state tree crown maps clearly indicate that mortality from the disease has spread well beyond the area of infection that in 2014 was restricted to the easternmost Puna District of Hawaii Island; currently, 'ōhi'a stands experiencing *Ceratocystis*-induced mortality are found on each of the five main volcanoes of the Island. Preliminary results from forest inventory plot data indicate that, on average, 'ōhi'a stands in which infected trees are present exhibit annual mortality rates of 10%, with some stands experiencing rates as high as 42% [42].

The final brown-state and leafless crown maps will support efforts to combat ROD throughout Hawaii Island, and on other islands if the disease is transported westward. Final maps show several hotspots where either the extent or the existence of infection was previously unknown. Recent developments have allowed the cause of death of these crowns to be rapidly confirmed as ROD using field kits that can genetically screen for *Ceratocystis* fungus [43]. The location of confirmed hotspots of ROD infections can help pathologists, ecologists, and land managers to better understand mechanisms of how ROD spreads, what regions are most vulnerable, and where and how to best allocate resources to reduce damage [8]. Additionally, research is underway to determine the feasibility of restoring 'ōhi'a to infected areas using genetic resistance techniques [44]. These maps will help to identify examples of 'ōhi'a trees that are that may be resistant to the *Ceratocystis* species causing the disease. As a single snapshot in time, these maps integrate the past progression of ROD across the 'ōhi'a forests of Hawaii Island. However, remapping the island using laser-guided imaging spectroscopy will enable a more-refined and up-to-date understanding of the rate of ROD proliferation. While the general methodology presented here can be readily transferred to such a remapping or any new applications, several specific facets of this methodology should be transferred with care. Just as highly-optimized models should not be blindly applied to new data—whether they come from different instruments, different time periods, or collected over different locations—the transferability of specific values in the classification rule or in the different post-processing filters will need to be reevaluated during each application as well.

5. Conclusions

Our results demonstrate that it is feasible to produce detailed, high-resolution maps of the likely extent of ROD outbreak at the level of individual tree crowns throughout native *Metrosideros polymorpha* ('ōhi'a) forests of Hawaii Island using airborne laser-guided imaging spectroscopy. By identifying [10] and compiling LGIS reflectance spectra of individual ROD-infected brown-state tree crowns and leafless crowns identified in the high-resolution color imagery, we found that these two tree conditions exhibit high spectral separability both from living tree canopies, as well as from one another. Via an

ensemble of two different machine learning algorithms, we accurately identified locations of potential ROD infection, both current (brown-state) and past (leafless), with minimal false detection. Such maps open a door to new research to aid in the effort to reduce the impact of Rapid 'Ōhi'a Death and to potentially restore 'ōhi'a forests already lost to this deadly pathogen.

Acknowledgments: This study was supported by funds from the U.S. Forest Service, Hawaii Department of Land and Natural Resources, Hawaii Department of Agriculture, Avatar Alliance Foundation, and the Carnegie Institution for Science. Field verification of maps was performed by Rob Hamnett, Nainoa Goo, Kalena Shiroma, and Kyson Dunn of the U.S. Forest Service, and Danny Duda of the U.S. Park Service. The Carnegie Airborne Observatory has been made possible by grants and donations to G.P. Asner from the Avatar Alliance Foundation, Margaret A. Cargill Foundation, David and Lucile Packard Foundation, Gordon and Betty Moore Foundation, Grantham Foundation for the Protection of the Environment, W. M. Keck Foundation, John D. and Catherine T. MacArthur Foundation, Andrew Mellon Foundation, Mary Anne Nyburg Baker and G. Leonard Baker Jr., and William R. Hearst III.

Author Contributions: Gregory P. Asner, Nicholas R. Vaughn, and R. Flint Hughes conceived and designed the experiments; Joseph W. Heckler and Gregory P. Asner performed the experiments; Nicholas R. Vaughn, Joseph W. Heckler, David E. Knapp, Philip G. Brodrick, and Roberta E. Martin analyzed the data; Nicholas R. Vaughn and Gregory P. Asner wrote the paper.

Conflicts of Interest: The founding sponsors had no role in the design of the study; in the collection, analyses, or interpretation of data; in the writing of the manuscript; or in the decision to publish the results.

References

1. Cordell, S.; Goldstein, G.; Mueller-Dombois, D.; Webb, D.; Vitousek, P.M. Physiological and morphological variation in *Metrosideros polymorpha*, a dominant Hawaiian tree species, along an altitudinal gradient: The role of phenotypic plasticity. *Oecologia* **1998**, *113*, 188–196. [CrossRef] [PubMed]
2. Martin, R.E.; Asner, G.P.; Sack, L. Genetic variation in leaf pigment, optical and photosynthetic function among diverse phenotypes of *Metrosideros polymorpha* grown in a common garden. *Oecologia* **2007**, *151*, 387–400. [CrossRef] [PubMed]
3. Friday, J.B.; Herbert, D.A. *Metrosideros polymorpha*. In *Traditional Trees of the Pacific Islands: Their Culture, Environment, and Use*; Elevitch, C.R., Ed.; Permanent Agriculture References: Hōlualoa, HI, USA, 2006; Volume 191, pp. 465–490.
4. Mortenson, L.A.; Flint Hughes, R.; Friday, J.B.; Keith, L.M.; Barbosa, J.M.; Friday, N.J.; Liu, Z.; Sowards, T.G. Assessing spatial distribution, stand impacts and rate of *Ceratocystis fimbriata* induced 'ōhi'a (*Metrosideros polymorpha*) mortality in a tropical wet forest, Hawai'i Island, USA. *For. Ecol. Manag.* **2016**, *377*, 83–92. [CrossRef]
5. Gruner, D.S. Arthropods From 'Ōhi'a Lehua (Myrtaceae: *Metrosideros polymorpha*). *Bish. Museum Occas. Pap.* **2004**, *78*, 33–52.
6. Stemmermann, L. Ecological studies of Hawaiian *Metrosideros* in a successional context. *Pac. Sci.* **1983**, *37*, 361–373.
7. Somers, B.; Asner, G.P. Invasive species mapping in hawaiian rainforests using multi-temporal hyperion spaceborne imaging spectroscopy. *IEEE J. Sel. Top. Appl. Earth Obs. Remote Sens.* **2013**, *6*, 351–359. [CrossRef]
8. Loope, L. Guidance Document for Rapid 'Ōhi'a Death. 2016. Available online: <https://gms.ctahr.hawaii.edu/gs/handler/getmedia.ashx?moid=4793&dt=3&g=12> (accessed on 21 March 2018).
9. Keith, L.M.; Hughes, R.F.; Sugiyama, L.S.; Heller, W.P.; Bushe, B.C.; Friday, J.B. First Report of *Ceratocystis* Wilt on 'Ōhi'a (*Metrosideros polymorpha*). *Plant Dis.* **2015**, *99*, 1276. [CrossRef]
10. Asner, G.P.; Martin, R.E.; Keith, L.; Heller, W.; Vaughn, N.R.; Hughes, R.F.; Balzotti, C. A Spectral Mapping Signature for the Rapid 'Ōhi'a Death (ROD) Pathogen in Hawaiian Forests. *Remote Sens.* **2018**, *10*, 404. [CrossRef]
11. Asner, G.P.; Knapp, D.E.; Boardman, J.; Green, R.O.; Kennedy-Bowdoin, T.; Eastwood, M.; Martin, R.E.; Anderson, C.; Field, C.B. Carnegie Airborne Observatory-2: Increasing science data dimensionality via high-fidelity multi-sensor fusion. *Remote Sens. Environ.* **2012**, *124*, 454–465. [CrossRef]
12. Asner, G.P.; Martin, R.E. Spectral and chemical analysis of tropical forests: Scaling from leaf to canopy levels. *Remote Sens. Environ.* **2008**, *112*, 3958–3970. [CrossRef]

13. Asner, G.P.; Martin, R.E.; Knapp, D.E.; Tupayachi, R.; Anderson, C.B.; Sinca, F.; Vaughn, N.R.; Llactayo, W. Airborne laser-guided imaging spectroscopy to map forest trait diversity and guide conservation. *Science* **2017**, *355*, 385–389. [[CrossRef](#)] [[PubMed](#)]
14. Cortes, C.; Vapnik, V. Support Vector Networks. *Mach. Learn.* **1995**, *20*, 273–297. [[CrossRef](#)]
15. Melgani, F.; Bruzzone, L. Classification of hyperspectral remote sensing images with support vector machines. *IEEE Trans. Geosci. Remote Sens.* **2004**, *42*, 1778–1790. [[CrossRef](#)]
16. Mountrakis, G.; Im, J.; Ogole, C. Support vector machines in remote sensing: A review. *ISPRS J. Photogramm. Remote Sens.* **2011**, *66*, 247–259. [[CrossRef](#)]
17. Baldeck, C.; Asner, G. Single-Species Detection with Airborne Imaging Spectroscopy Data: A Comparison of Support Vector Techniques. *IEEE J. Sel. Top. Appl. Earth Obs. Remote Sens.* **2014**, *8*, 2501–2512. [[CrossRef](#)]
18. Paz-Kagan, T.; Asner, G.P. Drivers of woody canopy water content responses to drought in a Mediterranean-type ecosystem. *Ecol. Appl.* **2017**, *0*, 1–14. [[CrossRef](#)] [[PubMed](#)]
19. Colgan, M.S.; Baldeck, C.A.; Féret, J.B.; Asner, G.P. Mapping savanna tree species at ecosystem scales using support vector machine classification and BRDF correction on airborne hyperspectral and LiDAR data. *Remote Sens.* **2012**, *4*, 3462–3480. [[CrossRef](#)]
20. Mason, L.; Baxter, J.; Bartlett, P.; Frean, M. Boosting algorithms as gradient descent. In Proceedings of the 12th International Conference on Neural Information Processing Systems, Denver, CO, USA, 29 November–04 December 1999; MIT Press: Denver, CO, USA; pp. 512–518.
21. Friedman, J.H. Greedy Approximation Function. *Ann. Stat.* **2001**, *29*, 1189–1232. [[CrossRef](#)]
22. Pedregosa, F.; Varoquaux, G. Scikit-learn: Machine learning in Python. *J. Mach. Learn. Res.* **2011**, *12*, 2825–2830. [[CrossRef](#)]
23. Clark, M.L.; Roberts, D.A.; Clark, D.B. Hyperspectral discrimination of tropical rain forest tree species at leaf to crown scales. *Remote Sens. Environ.* **2005**, *96*, 375–398. [[CrossRef](#)]
24. Gong, P.; Pu, R.; Yu, B. Conifer species recognition: An exploratory analysis of in situ hyperspectral data. *Remote Sens. Environ.* **1997**, *62*, 189–200. [[CrossRef](#)]
25. Asner, G.P. Biophysical and biochemical sources of variability in canopy reflectance. *Remote Sens. Environ.* **1998**, *64*, 234–253. [[CrossRef](#)]
26. De'ath, G. Boosted regression trees for ecological modeling and prediction. *Ecology* **2007**, *88*, 243–251. [[CrossRef](#)]
27. Niemiec, R.M.; Asner, G.P.; Brodrick, P.G.; Gaertner, J.A.; Ardoin, N.M. Scale-dependence of environmental and socioeconomic drivers of albizia invasion in Hawaii. *Landsc. Urban Plan.* **2018**, *169*, 70–80. [[CrossRef](#)]
28. Juvik, J.O.; Singleton, D.C.; Clarke, G.G. Climate and Water Balance on the Island of Hawaii. *Water Encycl.* **2005**, *4*, 255–263. [[CrossRef](#)]
29. Vitousek, P.; Asner, G.P.; Chadwick, O.A.; Hotchkiss, S. Landscape-level variation in forest structure and biogeochemistry across a substrate age gradient in Hawaii. *Ecology* **2009**, *90*, 3074–3086. [[CrossRef](#)] [[PubMed](#)]
30. Opitz, D.; Maclin, R. Popular Ensemble Methods: An Empirical Study. *J. Artif. Intell. Res.* **1999**, *11*, 169–198. [[CrossRef](#)]
31. Sharkey, A.J.C. Multi-Net Systems. In *Combining Artificial Neural Nets: Ensemble and Modular Multi-Net Systems*; Sharkey, A.J.C., Ed.; Springer: London, UK, 1999; ISBN 978-1-4471-0793-4.
32. Rokach, L. Ensemble-based classifiers. *Artif. Intell. Rev.* **2010**, *33*, 1–39. [[CrossRef](#)]
33. Friedman, J.H. Greedy Function Approximation: A Gradient Boosting Machine. *Ann. Stat.* **1999**, *1*, 1–10. [[CrossRef](#)]
34. Schapire, R.E. Measures of Diversity in Classifier Ensembles. *Mach. Learn.* **2003**, *51*, 181–207. [[CrossRef](#)]
35. Clark, P.E.; Rilee, M.L. Visible and Circumvisible Regions and Image Interpretation. In *Remote Sensing Tools for Exploration: Observing and Interpreting the Electromagnetic Spectrum*; Springer: New York, NY, USA, 2010; pp. 53–113, ISBN 978-1-4419-6830-2.
36. Clark, R.N.; Swayze, G.A.; Livo, K.E.; Kokaly, R.F.; King, T.V.V.; Dalton, J.B.; Vance, J.S.; Rockwell, B.W.; Hoefen, T.; McDougal, R.R. Surface Reflectance Calibration of Terrestrial Imaging Spectroscopy Data: A Tutorial Using AVIRIS. In *Proceedings of the 10th JPL Airborne Earth Science Workshop*; Jet Propulsion laboratory: Pasadena, CA, USA, 2002.
37. Barnsley, M.J.; Strahler, A.H.; Morris, K.P.; Muller, J. Sampling the surface bidirectional reflectance distribution function (BRDF): 1. Evaluation of current and future satellite sensors. *Remote Sens. Rev.* **1994**, *8*, 271–311. [[CrossRef](#)]

38. Vauhkonen, J.; Ene, L.; Gupta, S.; Heinzl, J.; Holmgren, J.; Pitkänen, J.; Solberg, S.; Wang, Y.; Weinacker, H.; Hauglin, K.M.; et al. Comparative testing of single-tree detection algorithms under different types of forest. *Forestry* **2012**, *85*, 27–40. [[CrossRef](#)]
39. Koch, B.; Heyder, U.; Weinacker, H. Detection of individual tree crowns in airborne lidar data. *Photogramm. Eng. Remote Sens.* **2006**, *72*, 357. [[CrossRef](#)]
40. Zhen, Z.; Quackenbush, L.J.; Zhang, L. Trends in Automatic Individual Tree Crown Detection and {Delineation—Evolution} of {LiDAR} Data. *Remote Sens.* **2016**, *8*, 333. [[CrossRef](#)]
41. Boehmer, H.J.; Wagner, H.H.; Jacobi, J.D.; Gerrish, G.C.; Mueller-Dombois, D. Rebuilding after collapse: Evidence for long-term cohort dynamics in the native Hawaiian rain forest. *J. Veg. Sci.* **2013**, *24*, 639–650. [[CrossRef](#)]
42. Hughes, R.F. (Insituition for Pacific Islands Forestry, USDA Forest Service). Unpublished data, 2017.
43. Atkinson, C.T.; Watcher-Weatherwax, W.; Roy, K.; Heller, W.P.; Kieth, L.M. *A Rapid Diagnostic Test. and Mobile “Lab. in a Suitcase” Platform for Detecting Ceratocystis spp. Responsible for Rapid ‘Ōhi’a Death*; HCSU: Hilo, HI, USA, 2017.
44. Hauff, R.D. Important Hawaiian tree species in need of genetic conservation. In *General Technical Report PNW-GTR-963, Proceeding of a Workshop: Gene Conservation of Tree Species—Banking on the Future*; Sniezko, R.A., Man, G., Hipkins, V., Woeste, K., Gwaze, D., Kliejunas, J.T., McTeague, B.A., Eds.; Pacific Northwest Research Station, USDA Forest Service: Portland, OR, USA, 2017; p. 1.



© 2018 by the authors. Licensee MDPI, Basel, Switzerland. This article is an open access article distributed under the terms and conditions of the Creative Commons Attribution (CC BY) license (<http://creativecommons.org/licenses/by/4.0/>).